Evaluation of Copper Vanadate (β-$Cu_2V_2O_7$) as a Photoanode Material for Photoelectrochemical Water Oxidation

Journal:	*Chemistry of Materials*
Manuscript ID	cm-2019-04909d.R3
Manuscript Type:	Article
Date Submitted by the Author:	n/a
Complete List of Authors:	Song, Angang; HZB, solar fuels Chemseddine, Abdelkrim; Helmholtz-Zentrum Berlin für Materialien und Energie GmbH, Inst. Solar Fuels (EE-IF) Ahmet, Ibbi; Helmholtz-Zentrum Berlin fur Materialien und Energie GmbH, Institute of Solar Fuels Bogdanoff, Peter; Helmholtz-Zentrum Berlin fur Materialien und Energie GmbH, Friedrich, Dennis; Helmholtz-Zentrum Berlin fur Materialien und Energie GmbH, Solar Fuels Abdi, Fatwa; Helmholtz-Zentrum Berlin fur Materialien und Energie GmbH, Institute for Solar Fuels Berglund, Sean; Helmholtz-Zentrum Berlin fur Materialien und Energie GmbH, van de Krol, Roel; Helmholtz-Zentrum Berlin fur Materialien und Energie GmbH, Institute for Solar Fuels

Evaluation of Copper Vanadate (β-$Cu_2V_2O_7$) as a Photoanode Material for Photoelectrochemical Water Oxidation

Angang Song,[ab] Abdelkrim Chemseddine,[a] Ibbi Yilmaz Ahmet,[a] Peter Bogdanoff,[a] Dennis Friedrich,[a] Fatwa F. Abdi,[a] Sean P. Berglund[a] and Roel van de Krol[ab]*

a. Institute for Solar Fuels, Helmholtz-Zentrum Berlin für Materialien und Energie GmbH, Hahn-Meitner-Platz 1, 14109 Berlin, Germany.

b. Institut für Chemie, Technische Universität Berlin, Straße des 17. Juni 124, 10623 Berlin, Germany.

ABSTRACT: Monoclinic copper vanadate (n-type $Cu_2V_2O_7$) thin film photoanodes were prepared for the first time by spray pyrolysis and evaluated for photoelectrochemical (PEC) water oxidation. The spray pyrolysis parameters were optimized to obtain phase pure photoanodes of β-$Cu_2V_2O_7$ (ziesite). The bandgap energy of β-$Cu_2V_2O_7$ is ~2.0 eV, which corresponds to a theoretical solar-to-hydrogen (STH) efficiency of 16% if it can be paired with an appropriate photocathode in a tandem device to drive overall water splitting. However, all $Cu_2V_2O_7$ photoanodes prepared so far have shown relatively low photoconversion efficiencies, and the properties that limit the efficiency have not yet been fully identified. In this work, many key physical and photoelectrochemical properties of β-$Cu_2V_2O_7$, such as optical band gap, doping type, flat-band potential, band positions, charge carrier dynamics, and chemical stability are reported. The photoelectrochemical performance of the β-$Cu_2V_2O_7$ photoanodes is found to be limited by a short carrier diffusion length and slow water oxidation kinetics. Time-resolved microwave conductivity (TRMC) measurements reveal that the short carrier diffusion length (~28 nm) is mainly due to a relatively low carrier mobility (~3.5×10^{-3} cm^2 V^{-1} s^{-1}). The slow water oxidation kinetics can be improved by using cobalt phosphate (CoP_i) as a water oxidation co-catalyst, resulting in a doubling of the photocurrent.

INTRODUCTION

The development of metal oxide semiconductor photoelectrodes for photoelectrochemical (PEC) water splitting is regarded as a promising way to generate renewable energy mainly due to their potential for relatively low-cost fabrication and chemical stability.[1-3] Generally, an "ideal" semiconductor material should possess a band gap of 1.6 – 2.1 eV in order to absorb the maximum amount of visible light and to provide the necessary potential to drive the water splitting reaction.[4] Further, the charge carriers must be effectively separated and easily transported from the bulk to the material's surface for water reduction or oxidation.[5] In addition, the photoelectrode's conduction and valence bands should straddle the proton reduction and water oxidation redox potentials.[6] A tandem cell approach would help to meet these demands and is widely accepted to be a promising approach. With a bandgap of 1.12 eV, silicon would be a nearly ideal bottom absorber when combined with a top absorber with a bandgap of ~1.8 eV.

So far, many earth-abundant metal oxides have been studied as potential top absorbers and only some of them have attracted lasting attention of researchers for water oxidation applications. Well-studied examples are hematite (α-Fe_2O_3), $BiVO_4$, TiO_2 and WO_3.[7-10] However, STH efficiencies are still much lower than target values because of either a too large bandgap, poor carrier diffusion length, and/or poor surface reactivity. Therefore, finding an efficient and stable metal oxide absorber with a suitable bandgap would be a major breakthrough for the photoelectrochemical (PEC) water splitting field.

From a combination of high-throughput theory and experiments, the metal vanadates were identified as a potentially promising class of materials.[11] Within this class, a number of interesting complex metal oxide phases exists within the CuO-V_2O_5 system. It is known that by stoichiometric variation of the Cu to V ratio in the $Cu_xV_yO_z$ system a number of temperature dependent stoichiometric phases and polytypes can exist.[12, 13] Of these, the high temperature orthorhombic α-$Cu_2V_2O_7$ (blossite) and low temperature monoclinic β-$Cu_2V_2O_7$ (ziesite) polymorphs have been identified as potential photoanode materials.[14-16] Both polymorphs are n-type metal oxide semiconductors, which have been reported to have suitable indirect and direct optical band gaps in the range of 1.8 – 2.1 eV and moderate absorption coefficients (up to $\alpha \approx 10^4$ cm^{-1}), allowing for the utilization of a significant portion of the solar spectrum for the generation of photocurrent.[17-21] With a band gap close to 2.0 eV, a calculated maximum theoretical photocurrent density of ~15 mA cm^{-2} is achievable under AM1.5 illumination, assuming all photons with energies higher than the bandgap are absorbed and utilized with 100% efficiency.[22, 23] However, the experimental AM 1.5 photo current densities reported so far for the α-$Cu_2V_2O_7$ (blossite) and

β-$Cu_2V_2O_7$ (ziesite) polymorphs have been well below this theoretical limit. Furthermore, an incomplete understanding of the limitations for this material system remains.

In this work, a straightforward spray pyrolysis procedure is developed for the deposition of the low temperature β-$Cu_2V_2O_7$ (ziesite) polymorph as thin films on FTO-coated glass (F-doped SnO_2) and quartz substrates. Subsequently, the key physical and photoelectrochemical properties relevant to PEC water oxidation such as optical absorption, doping type, flatband potential, band positions, charge carrier dynamics, and chemical stability are reported. On the basis of these findings, we will identify the factors that limit the performance of $Cu_2V_2O_7$ as a photoanode material for solar water splitting and discuss remaining challenges and appropriate strategies to overcome these limitations.

EXPERIMENTAL SECTION

Photoanode Synthesis

$Cu_2V_2O_7$ thin film photoanodes were prepared using the following low-cost and facile spray pyrolysis process. First, 20 mM $Cu(NO_3)_2$ precursor was prepared by dissolving $Cu(NO_3)_2{\cdot}3H_2O$ (99–104%, Sigma-Aldrich) in ethanol (≥99.8%, Sigma-Aldrich). Next 20 mM $VO(AcAc)_2$ precursor was prepared by dissolving $VO(C_2H_7O_2)_2$ (99%, Alfa Aesar) in absolute ethanol. The Cu solution was then added to the V solution, and the mixture was diluted to the desired concentration with additional ethanol. The substrates (FTO-coated glass, 7 Ω per square, TEC-7, Pilkington) were cleaned by three successive 15 min ultrasonic treatments in a Triton™ X-100 solution, acetone, and ethanol. The substrates were placed on a hot plate heated to the preset temperature of 300 °C. A Quickmist collision atomizer was placed 20 cm above the substrate. The atomizer was controlled with an overpressure of ~2.5 bar of nitrogen gas to achieve a spray rate of 2.0 mL per 5 s spray. The spray cycle consisted of 5 s spray followed by a 55 s pause, allowing for the evaporation of the solvent and the pyrolysis of any remaining organic components. The spray cycle was repeated 100 times and a film growth rate of 2 nm per cycle was determined.

After deposition, the $Cu_2V_2O_7$ thin film photoanodes were placed in muffle furnace that was exposed to air. The temperature was ramped at a rate of 5 °C/min to 500 °C and the films were annealed at that temperature for 2 hours. The samples were cooled using natural convection.

The CoP_i catalyst was electrodeposited (in the dark) on $Cu_2V_2O_7$ photoanodes at 0.9 V versus Ag/AgCl for 30 s (see Figure S1a) in an electrochemical cell consisting of an aqeuous solution of 0.5 mM of $Co(NO_3)_2.6H_2O$ in 0.3 M K_2SO_4 and 0.2 M phosphate buffer (pH 6.8) using a three-electrode configuration.[24, 25] Three linear sweep voltammetry (LSV) cycles were performed under illumination in order to activate the CoP_i-modified $Cu_2V_2O_7$ photoanodes as shown in Figure S1b.

Material Characterization

X-ray diffraction (XRD) measurements were performed with a Bruker D8 diffractometer using Cu K_α radiation (λ= 0.15406 nm). The X-ray tube was operated at an acceleration voltage of 40 kV and a current of 40 mA. A step size of 0.02° was used, with an integration time of 3.5 s/step. The top view and cross section images of the samples were captured using a LEO GEMINI 1530 field emission scanning electron microscope (FESEM) with an acceleration voltage of 7 kV for imaging. Using the same FESEM equipped with a silicon drift detector (Thermo Fisher Scientific), energy-dispersive X-ray analysis (EDX) was conducted with an acceleration voltage of 20 kV. The surface morphologies of the samples were investigated by atomic force microscopy (AFM) using a Park Systems XE-100 AFM operating in tapping mode. A Si tip with a radius of 10 nm and a force constant of 40 N/m was used. All scans were performed on a scale of 5 μm × 5 μm with the laterally resolved height information mapped on a square array of 256 × 256 pixels. UV-vis absorption spectra were measured using a PerkinElmer Lambda 950 spectrometer fitted with an integrating sphere. The short-range structure and vibrational modes were analyzed by Raman spectroscopy (Dilor Micro LabRAM, Horiba) with a laser excitation wavelength of 635 nm and a power of 0.6 mW at the objective (spot size: ~1 μm in diameter). X-ray photoemission spectroscopy (XPS) and ultraviolet photoelectron spectroscopy (UPS) were conducted using a system developed in house under ultrahigh vacuum with a base pressure of $\sim 10^{-8}$ mbar. The films were cleaned in an oxygen plasma (4×10^5 mbar, 99.999%, 200 W) prior to analysis in order to remove carbon species adsorbed at the surface. XPS was performed with a monochromatic Al Kα X-ray source (1486.74 eV) with a SPECS Focus 500 monochromator. The analyzer was supplied by SPECS (Phoibos 100) and a source-to-analyzer angle of 54° was used. UPS was performed with a He I source (E = 21.21 eV) and two measurements were conducted in which the ground of the sample holder was used to subject the sample to 0 V and 2 V bias voltages. All spectra were measured using a pass energy and step size of 10 and 0.05 eV, respectively. For data analysis the 1s peak of adventitious carbon at 284.8 eV was used as a reference for the other peak positions (see Figure S2b).

Time-resolved microwave conductivity (TRMC) measurements were performed using a wavelength-tunable optical parametric oscillator (OPO) coupled to a frequency-tripled diode-pumped Q-switched Nd:YAG laser at wavelengths of 405, 450, and 550 nm as the excitation source with a 3 ns pulse width (full-width at half maximum) and a X-band (8400–8700 MHz) microwave probe. The sample was placed in a cavity to enhance the sensitivity; within the cavity, it was exposed to ambient air. The charge carrier diffusion lengths (L_D) were calculated using the following relationship,

$$L_D = \sqrt{\left(\frac{\mu k T}{q}\right)\tau} \quad (1)$$

where μ is mobility ($m^2\ V^{-1}\ s^{-1}$), k is the Boltzmann constant, T is the temperature (K), q is the electronic

charge (1.602×10^{-19} C), and τ is the charge carrier lifetime (s).

Photoelectrochemical and Electrochemical Characterization

Photoelectrochemical measurements were based on the procedures described in our previous work.[26] The measurements were performed in three-electrode cell controlled by a potentiostat (EG&G Princeton Applied Research 273A). The sample was connected as the working electrode while a Pt wire was used as the counter electrode. An Ag/AgCl electrode (saturated KCl) was used as the reference electrode. Photocurrent measurements were carried out in an aqueous electrolyte of 0.3 M K_2SO_4 and 0.2 M phosphate buffer (pH 6.8). The pH was measured with a pH meter (OAKTON). A WACOM super solar simulator (Model WXS-50S-5H, class AAA) was used as the illumination source. The solar simulator was calibrated to closely match the AM1.5 global spectrum at 100 mW/cm^2, especially in the UV region (350-400 nm). All of the measured potentials were converted to the reversible hydrogen electrode (RHE) scale using the Nernstian relation:

$$V_{RHE} = V_{Ag/AgCl} + 0.059(\mathrm{V}) \times pH + 0.197(V) \quad (2)$$

Incident photon-to-current conversion efficiency (IPCE) and absorbed photon-to-current efficiency (APCE) measurements were performed with a 300 W xenon lamp (Oriel) connected to a grating monochromator (Acton Spectra Pro 2155). The IPCE and APCE were calculated from the following formulas:

$$IPCE = \frac{J_{pho}(\lambda)}{P(W)} \times \frac{1240}{\lambda} \times 100\% \quad (3)$$

$$APCE = \frac{IPCE\,\%}{A} \quad (4)$$

Where J_{pho} is the average photocurrent (mA/cm^2), P is power density of the light incident on the photoanode (mW cm^{-2}), λ is the wavelength (nm), and A is the absorptance of the $Cu_2V_2O_7$ photoanode. Figure S3 shows power spectra for front illumination IPCE measurements. The IPCE measurements were done at 1.23 V vs. RHE with or without CoP_i as catalyst. The predicted AM1.5 photocurrent density ($J_{AM1.5}$) of the photocathodes was estimated by multiplying the IPCE values by the AM1.5 solar photon flux and the electronic charge and subsequently integrating this for wavelengths below 700 nm according to the following relationship,

$$J_{AM1.5} = \int_{300\,nm}^{700\,nm} (IPCE(\lambda) \times \Phi_{AM1.5}(\lambda) \times q)\, d_\lambda \quad (5)$$

where $J_{AM1.5}$ is the total solar photocurrent in (A m^{-2}), λ is the wavelength of the light (nm), $\Phi_{AM1.5}(\lambda)$ is the photon flux of AM1.5 sunlight (photons m^{-2} s^{-1}), and q is the electronic charge.

Electrical impedance spectroscopy (EIS) and Mott-Schottky measurements were performed with a VersaSTAT 3 Potentiostat (AMETEK Co., Ltd.). EIS was performed in the dark near the flat band potential (Figure S4), using a modulation amplitude of 5 mV. Mott–Schottky plots were fitted based on the following relationship,

$$\frac{1}{C^2} = \frac{2}{q\,\varepsilon\,\varepsilon_0\,N_D}\left(\varphi - \varphi_{fb} - \frac{k\,T}{q}\right) \quad (6)$$

where C is the space charge capacitance (F/m^2), ε is the relative permittivity or dielectric constant, ε_0 is the permittivity of free space, N_D is the donor density (m^{-3}), φ is the applied electrochemical potential (V), and φ_{fb} is the flat band potential. A dielectric constant of 500 was used for $Cu_2V_2O_7$ photoanodes.[27] The space charge width (W_{sc}) was estimated using the following expression.

$$W_{sc} = \sqrt{\frac{2\,\varepsilon\,\varepsilon_0}{q\,N_D}\left(\varphi - \varphi_{fb} - \frac{k\,T}{q}\right)} \quad (7)$$

For gas detection, electrochemical mass spectrometry measurements were carried out in a PEC cell with a 200 nm $Cu_2V_2O_7$ photoanode as the working electrode, a Pt wire as the counter electrode, and an Ag/AgCl reference electrode. To calibrate the measurements, a Pt sheet was used as the working electrode, and a calibration line was recorded for the gas signal as a function of the current (see Figure S5 in the Supporting Information). For a specific current, the Faradaic efficiency (η_F) for the photoanode could then be calculated using the following equation, under the assumption that the Pt sheet has 100% Faradaic efficiency for the oxygen evolution reaction:

$$\eta_F = \frac{O_2 \text{ signal from photoanode}}{O_2 \text{ signal from Pt sheet}} \times 100\% \quad (8)$$

After each mass spectrometry measurement the electrolyte was refreshed to avoid undesired shifts in the pH.

RESULTS AND DISCUSSION

Structural and morphology characterization

XRD, Raman spectroscopy, SEM, and EDX measurements were used to gain information on the structure, chemical composition, and morphology of deposited films. Figure 1a shows the XRD patterns for a bare FTO-coated glass substrate and a $Cu_2V_2O_7$ photoanode synthesized by spray pyrolysis on FTO-coated glass at 300 °C, followed by annealing in air at 500 °C. Also included at the bottom of the graph are the reference patterns of β-$Cu_2V_2O_7$ (ziesite, PDF no. 73-1032, asterisks) and SnO_2 (cassiterite, PDF no. 00-046-1088, solid diamonds). Ziesite has been reported to have a monoclinic crystal structure with the space group C2/c, unit cell parameters a = 7.685 Å, b = 8.007 Å, c = 10.09 Å and β = 110.27°.[28-31] The X-ray diffractogram for the prepared film matches very well with the reference pattern for β- $Cu_2V_2O_7$. There was no secondary phase detected for films with a thickness ranging from 50 to 400 nm (see Figure S6).

The chemical structure of the $Cu_2V_2O_7$ films was confirmed based on the Raman scattering data shown in Figure 1b. The Raman peaks observed at 392, 847, and 914 cm-1 can be attributed to the vibrations of the bonds in β-$Cu_2V_2O_7$.[18, 32, 33] The peak centered at 914 cm^{-1} is the characteristic band assigned to the VO_3 stretching mode.[34] No peaks corresponding to the V_2O_5 and CuO phase were detected, which confirms the phase purity of our $Cu_2V_2O_7$ films.

The $Cu_2V_2O_7$ photoanodes were inspected visually by eye and under magnification using a scanning electron

microscope (SEM). A photograph of a thin film $Cu_2V_2O_7$ photoelectrode deposited on an FTO-coated glass substrate after annealing at 500°C is shown in Figure S7. The film has a dark brown color, indicating good visible light absorption.

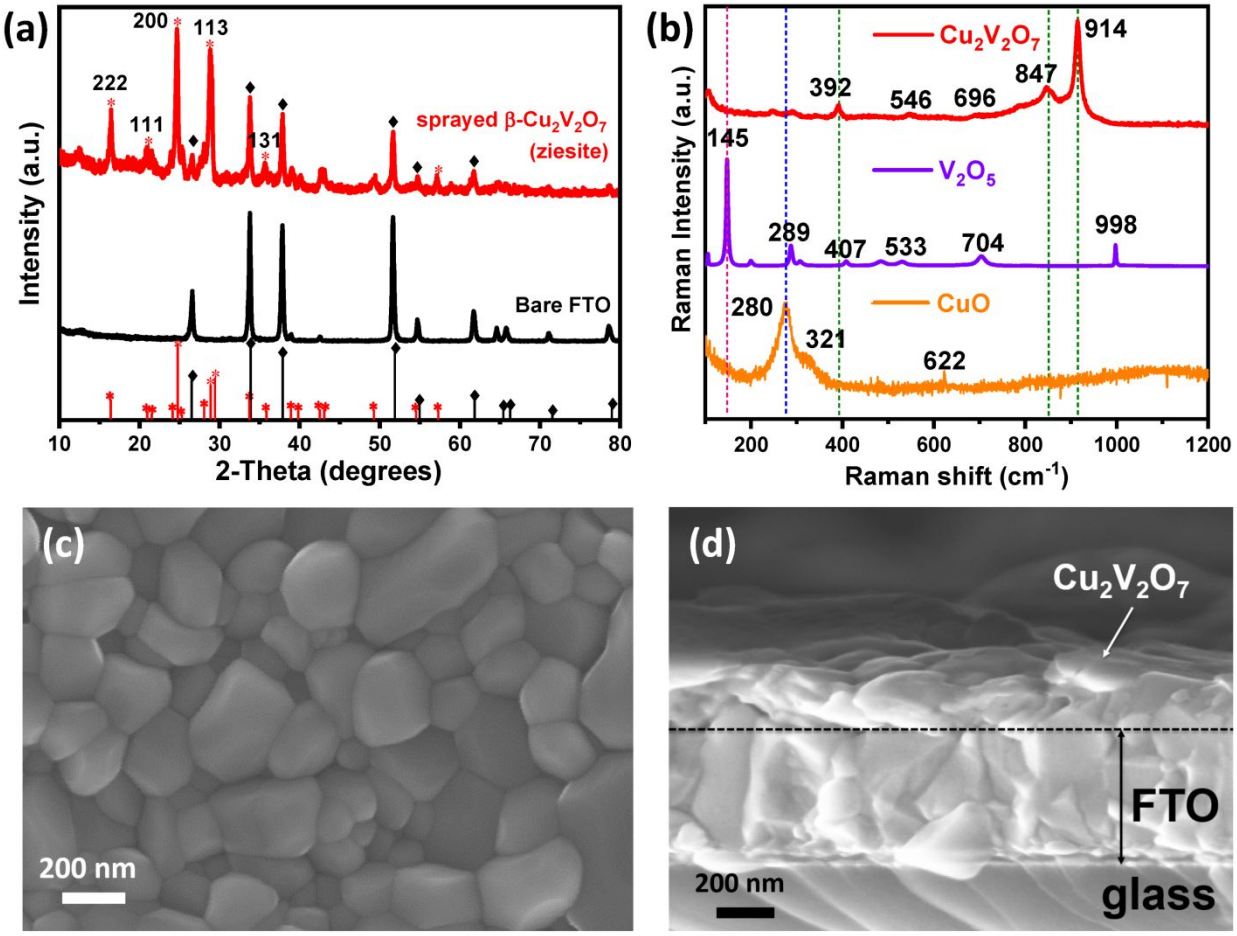

Figure 1. (a) X-ray diffractogram for a $Cu_2V_2O_7$ photoanode synthesized by spray pyrolysis on a FTO substrate and annealed at 500°C for 2 hours in air. Red vertical lines (*) represent the reference pattern for $Cu_2V_2O_7$ (PDF no. 73-1032) and black vertical lines (♦) represent the reference pattern for SnO_2 (PDF no. 00-046-1088) with line lengths proportional to peak intensities. (b) Raman spectrum of the same $Cu_2V_2O_7$ film. (c) Top view and (d) cross-sectional view SEM images of the $Cu_2V_2O_7$ film deposited on FTO and annealed at 500°C for 2 hours in air.

The as-deposited films consist of grains with roughly spherical or oblong shapes and with some degree of surface roughness as shown in Figure S8. Figure 1c shows the morphology of a $Cu_2V_2O_7$ film after annealing at 500°C in air. The grains exhibit well defined edges and have a relatively broad size distribution (50 – 400 nm). The cross-sectional SEM images were used to estimate the thickness of the $Cu_2V_2O_7$ films for different amounts of sprayed precursor volume. The thicknesses of the films prepared using 100, 200, and 300 mL precursor solution are found to be ~100, ~200, and ~300 nm as shown in Figures S9a, 1d, and S9b, respectively. This indicates a linear relationship between the sprayed precursor volume and the film thickness, with an average deposition efficiency of 1 nm per mL of spray solution.

The chemical composition of the annealed films was analysed by EDX mapping of a representative film area. The resulting SEM images with EDX mapping overlays are shown in Figure S10. The EDX signals from Cu, V, and O appear to be homogeneously distributed over the entire film area. The average atom ratio of Cu to V is about 1 to 1 (23.5 at. % Cu and 23.6 at. % V), which is expected from the phase-pure $Cu_2V_2O_7$ phase indicated by XRD.

The surface roughness of the $Cu_2V_2O_7$ photoanodes was measured using atomic force microscopy (AFM) as shown in Figure S11. AFM reveals that the root mean squared (RMS) roughness and the resulting surface area enhancement of $Cu_2V_2O_7$ films deposited directly on FTO are 50 nm and ~ 3%, respectively.

Optical absorption properties

The optical properties of the $Cu_2V_2O_7$ thin films synthesized by spray pyrolysis were investigated with UV–vis spectroscopy. The transflectance of these films, which is the sum of the tranmission and the reflection intensities, was measured by placing the sample inside the integrating sphere (at its center) to determine the true absorptance (absorptance = 1 – transflectance). Figure 2a shows the absorptance spectra of 200 nm $Cu_2V_2O_7$ thin film deposited on quartz as a function of wavelength (absorptance spectra for other thicknesses are shown in Figure S12a). The absorption edge is located at about 650

nm. The absorption coefficient (α) of the films can be calculated by using the following equation:

$$\alpha = (-\ln(1-A))/d \quad (9)$$

Here, A is the absorptance at a single wavelength and d is the film thickness. Figure 2b shows absorption coefficient as a function of photon energy (wavelength), which was calculated from a fit of the absorption data of 6 different film thicknesses. An example of an individual fit is shown in Figure S12b for a wavelength of 450 nm, for which an absorption coefficient of (3.35 ± 0.14) × 10^4 cm^{-1} is found. This corresponds to a light penetration depth of α^{-1} = 298 nm, which is the depth of the film at which more than 63% of the incident light has been absorbed. In order to absorb 90% of the incident light having a wavelength of 450 nm, a $Cu_2V_2O_7$ film thickness of 687 nm (2.3 α^{-1}) is required.

To extract the bandgap of $Cu_2V_2O_7$, Tauc plots are calculated based on the absorption coefficient spectrum and shown in Figure 2c. However, neither the direct nor indirect Tauc plot shows a steep, linear section that would allow for extrapolation to a bandgap value. One possible reason for this is the occurrence of intra-atom transitions between occupied and empty Cu 3d states, which may partially obscure the valence-to-conduction band transitions.[35] Another possible reason is the surface roughness of the films (Figure S11); the optical scattering may reduce the quality of the Tauc plots, even when the absorption spectra are recorded in an integrating sphere. Nevertheless, a rough estimate for the indirect and direct bandgaps for the $Cu_2V_2O_7$ thin film can be made, yielding values of 1.91 and 2.05 eV, respectively. This is consistent with previously reported values.[12, 35] However, even at photon energies below 1.9 eV the (apparent) absorption is ~10% (α = 5 × 10^3 cm^{-1}). While this may be partially due to scattering, the increasing value at lower photon energies could also indicate band tailing and/or free carrier absorption.

Charge carrier mobility and lifetime

Since the charge carrier transport in the bulk material plays a crucial role in the PEC process, time-resolved microwave conductivity (TRMC) was used to investigate the charge transport dynamics in $Cu_2V_2O_7$. In TRMC, the photo-induced conductivity changes of a sample are measured and expressed as $\phi\Sigma\mu$, where ϕ is the absorptance-normalizedquantum yield and $\Sigma\mu$ is the sum of the electron and hole mobilities. The combined carrier (electron and hole) mobility of the semiconductor is at least as high as the peak in the measured signal, since this is where ϕ is closest to its maximum value of 1.[36-39] Figure 3a shows the TRMC signal for a 200 nm $Cu_2V_2O_7$ film that was synthesized by spray pyrolysis on a quartz substrate. The excitation wavelength is 450 nm and the measurements were done for various incident laser pulse intensities. Carrier mobilities between 3.4 × 10^{-3} and 4.1 × 10^{-3} cm^2 V^{-1} s^{-1} are obtained for laser pulse intensities between 5.4 × 10^{14} and 9.5 × 10^{14} photons cm^{-2}.

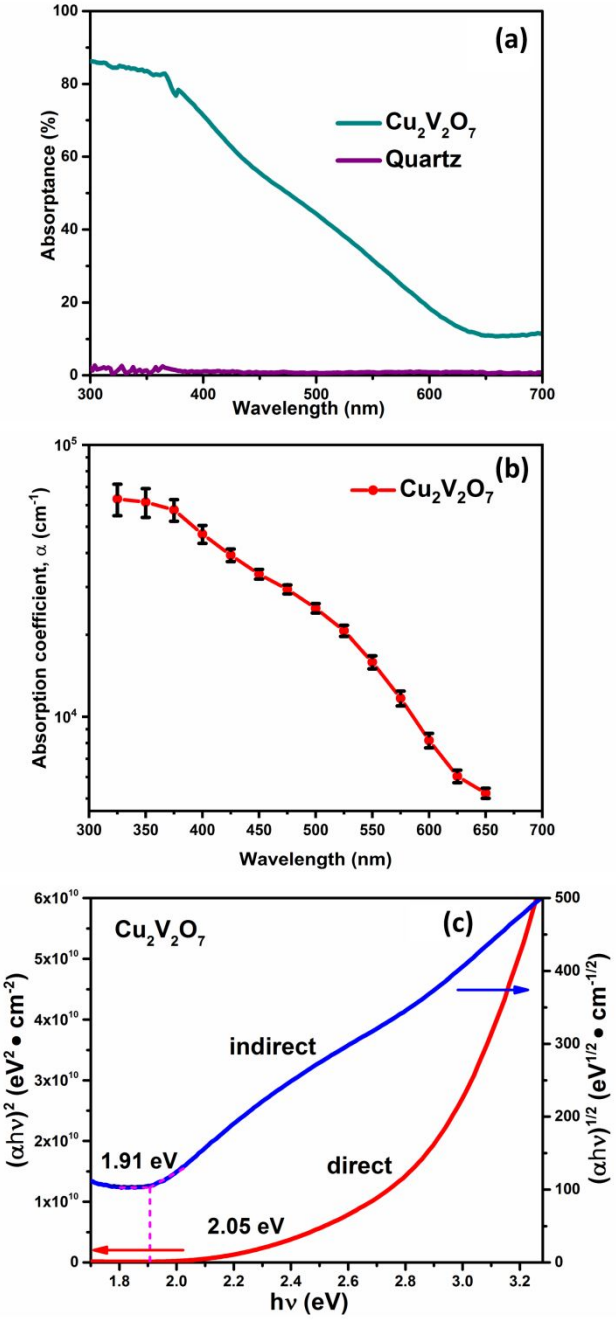

Figure 2. (a) Absorptance spectra for $Cu_2V_2O_7$ film deposited on quartz substrate and annealed at 500°C for 2 hours in air with estimated thicknesses of 200 nm as determined by cross-sectional SEM images, (b) absorption coefficient for the $Cu_2V_2O_7$ film plotted as a function of wavelength. The error bars represent the standard errors reported by the fitting procedure. (c) Tauc plot for bandgap analysis of the $Cu_2V_2O_7$ film. The indirect and direct bandgaps are estimated from the intercepts with the baselines of the low-energy parts of the curve.

The decay curves fit well with the power law $\phi\Sigma\mu = \gamma \times t^k$ over a time window ranging from ns to 10 μs, with γ = 1.9 × 10^{-5} and k = -0.33. This power-law behavior is generally observed for trapping-detrapping models[40, 41] and a strong

indication of trap-limited recombination in our films.[42-44] The TRMC signals at other wavelengths (405 nm and 550 nm) under various incident laser pulse intensities were also measured and shown in Figure S13. The mobility values for the $Cu_2V_2O_7$ film measured at various wavelengths were all of the same order of magnitude, ranging from 3.0×10^{-3} to 4.7×10^{-3} cm^2 V^{-1} s^{-1}.

Figure 3b shows the maximum values of the TRMC signals, $(\phi\Sigma\mu)_{max}$, versus incident laser pulse intensity. The $(\phi\Sigma\mu)_{max}$ signal gradually decreases with increasing light intensity for 450 and 550 nm excitation, which has been attributed to nongeminate higher order electron–hole recombination.[38] The effective lifetime of the charge carriers in the $Cu_2V_2O_7$ film can be defined as the time that it takes for the signal to decrease by 50% of its starting value, which results in an average value of 80 ns for our $Cu_2V_2O_7$ films. Based on this effective lifetime and an average mobility of 4×10^{-3} cm^2 V^{-1} s^{-1} (Fig. 3b), an effective charge carrier diffusion length can be calculated with Eq. (1). A value of ~28 nm is found for our $Cu_2V_2O_7$ films. It should be realized, however, that the interpretation of this "effective" value is somewhat ambiguous due to the role of carrier trapping and detrapping during the recombination process (see above).

To the best of our knowledge this is the first time that the effective carrier lifetime, mobility, and effective diffusion length for $Cu_2V_2O_7$ thin films have been reported. Interestingly, a similar value of the (hole) diffusion length (20-40 nm) was reported for γ-$Cu_3V_2O_8$.[23] For these and many other metal oxides, the effective carrier diffusion lengths are much shorter than the light penetration depth, α^{-1}. This means that most electron–hole pairs in bulk $Cu_2V_2O_7$ films will recombine before reaching the semiconductor/electrolyte interface, resulting in modest charge carrier separation efficiencies. We will discuss strategies to overcome this limitation in the following sections.

Photoelectrochemical properties

In order to investigate the photoelectrochemical activity of the sprayed $Cu_2V_2O_7$ films, chopped linear sweep voltammetry (LSV) measurements were conducted under simulated AM1.5 illumination (Figure 4a). For the water oxidation experiments, argon bubbling was used to remove dissolved O_2. The current–voltage (J–V) curves show moderate photocurrents, but a relatively positive onset potential of ~0.65 V vs. RHE. Photoelectrochemical measurements were performed systematically by varying the thicknesses of the thin film (50 – 400 nm) in order to optimize the performance of bare $Cu_2V_2O_7$ photoanodes as shown in Figure S14b. The maximum photocurrent was 0.05 mA/cm^2 at 1.23 V versus RHE for a film thickness of 200 nm. After depositing a CoP_i co-catalyst layer on top of the $Cu_2V_2O_7$ photoanodes, the photocurrent doubles to 0.1 mA/cm^2 at 1.23 V versus RHE for a 200 nm film. This is one of the highest photocurrent densities reported for an undoped $Cu_2V_2O_7$ photoelectrode.[17, 18] The improvement due to the CoPi was consistent for both frontside and backside illumination (see Figure S14a) and held for a range of $Cu_2V_2O_7$ film thicknesses between 50 and 400 nm as shown in the inset of Figure 4a (see Figure S14c for the individual LSV scans for different $Cu_2V_2O_7$ film thicknesses).

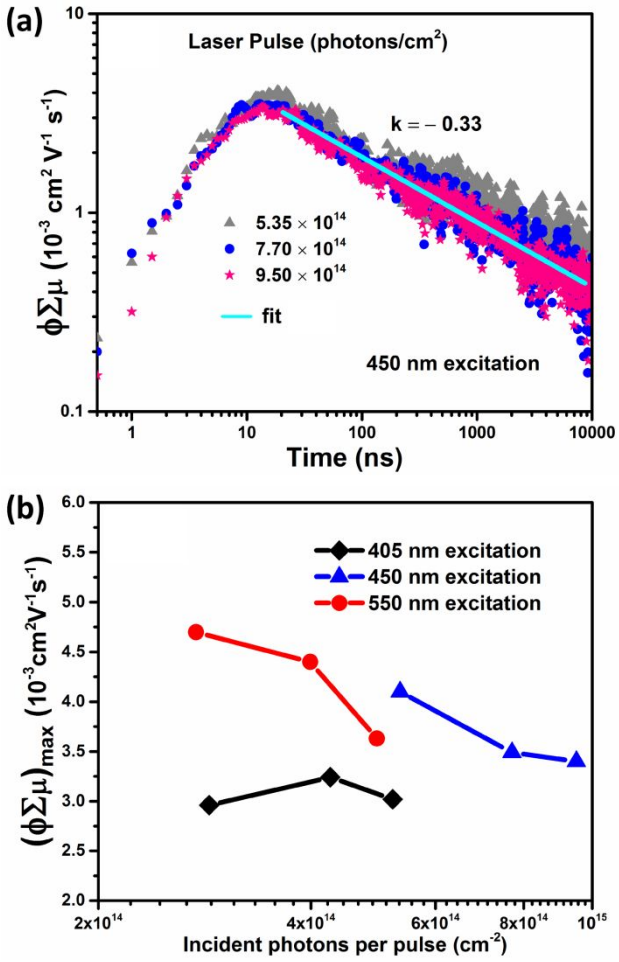

Figure 3. (a) TRMC signal under various incident laser pulse intensities for a $Cu_2V_2O_7$ film synthesized by spray pyrolysis on a quartz substrate at 450 nm wavelength. (b) Maximum TRMC signal $(\phi\Sigma\mu)_{max}$ vs incident laser pulse intensity for $Cu_2V_2O_7$ films for three different excitation wavelengths.

The quantum efficiency of $Cu_2V_2O_7$ photoanodes was determined by measuring the incident photon-to-current conversion efficiency (IPCE, also called external quantum efficiency, EQE) and the absorbed photon-to-current efficiency (APCE, or internal quantum efficiency). Figure 4b shows IPCE spectra of the $Cu_2V_2O_7$ films without and with CoP_i, measured at 1.23 V versus RHE. Consistent with the J–V curve analysis, the photoanode with CoP_i shows a higher IPCE value than the electrode without a co-catalyst for all wavelengths. However, the IPCE values are still very low, we achieve only 2.9% and 1.2% at 1.23 V vs RHE at a wavelength of 350 nm for the $Cu_2V_2O_7$ photoanodes with and without CoP_i, respectively. The IPCE values under backside illumination are even lower at 0.9% and 0.4%, respectively (Figure S14d).

The IPCE values can also be used to predict the AM1.5 photocurrent density ($J_{AM1.5}$) according to equation (5) in the Experimental section. For frontside illumination the predicted $J_{AM1.5}$ values are 0.097 mA/cm^2 and 0.041 mA/cm^2 at 1.23 V_{RHE} for the $Cu_2V_2O_7$ photoanodes measured with and without CoP_i, respectively, which are indeed very close to the values of 0.1 mA/cm^2 and 0.05 mA/cm^2 obtained for the chopped LSV measurements under AM1.5 solar simulation (see Figure S14f).

Figures S15a and S15b show the APCE spectra for $Cu_2V_2O_7/CoP_i$ photoanodes measured under front and back illumination, respectively. In both cases, the $Cu_2V_2O_7$ photoanodes with CoP_i exhibit a significantly higher APCE value than those without CoP_i for all wavelengths. Since the $Cu_2V_2O_7/CoP_i$ films show the same photocurrent as the bare $Cu_2V_2O_7$ films in the presence of a sodium sulfite hole scavenger (Figure S14e), the injection efficiency of the $Cu_2V_2O_7/CoP_i$ films must be close to 100%. Under these conditions, the APCE represents the charge separation efficiency. The APCE is 3.5% and 1.4% at 350 nm for the $Cu_2V_2O_7$ photoanodes measured with and without CoP_i, respectively. Thus, the CoP_i co-catalyst indeed improves the charge separation efficiency by enhancing the surface reaction kinetics and/or by reducing surface recombination. Nevertheless, the charge separation efficiencies are still very low.

We note that one distinct feature of the IPCE is the sharp increase at wavelengths below 350 nm. This has also been observed in previous reports on β-$Cu_2V_2O_7$ and is often found in other copper based metal oxide photo-electrodes with indirect band gaps.[17] One possible explanation is that at lower wavelengths, the penetration depth of the incident light decreases enough to become similar to the sum of the space charge layer width, W, and the carrier diffusion length, L_D. According to the Gärtner model, which assumes perfect charge separation within (W+L_D), this would indeed lead to an increase in the carrier collection efficiency. To check this, we used the absorption coefficient and the values for W (70 nm, see below) and L_D (28 nm) to calculate the IPCE using the Gärtner model. The results of the simulated IPCE, shown in Figure S16a, show that the increase at lower wavelengths is much more gradual than the experimental data in Figure S15. This suggests that the Gärtner model is not able to desribe the behavior of our films and that there are factors other than simply the location at which carriers are generated that determine the carrier collection efficiency.

Recent work on hematite photoanodes showed that the spectral dependence of the carrier collection efficiency can also be due to either[45] (i) wavelength-dependent carrier mobility or lifetime[46] or (ii) a wavelength-dependent carrier generation yield.[47] Since the TRMC shows that there is only minor wavelength dependency on the carrier mobility and lifetime in $Cu_2V_2O_7$, we attribute the sharp increase in the IPCE of $Cu_2V_2O_7$ below 350 nm to a wavelength-dependent photogeneration yield in this material. Indeed, the first electronic transition in $Cu_2V_2O_7$ is a Laporte-forbidden Cu d→d transition,[31, 35] like in hematite. It has been suggested that such transitions do not significantly contribute to the photocurrent. At higher photon energies, the O 2p → Cu 3d transition can occur, which would lead to a much stronger contribution to the photocurrent.

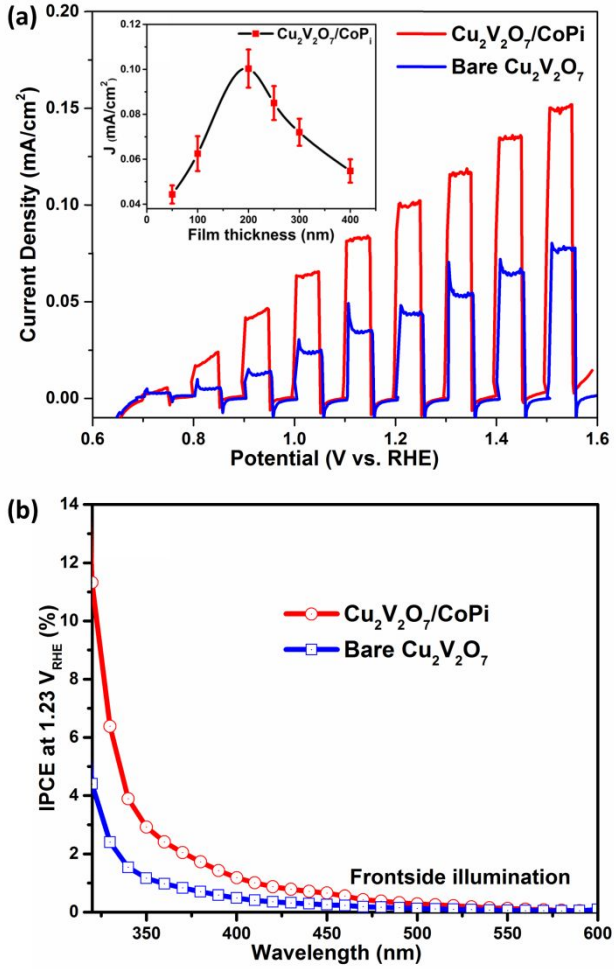

Figure 4. (a) Chopped LSV scans for 200 nm $Cu_2V_2O_7$ photoanodes on FTO without (blue line) and with CoP_i as a co-catalyst (red line). The inset shows the average photocurrent densities (at least 3 samples) at 1.23 V vs RHE extracted from LSV scans for photoanodes with CoP_i as a co-catalyst at different thicknesses (see Figure S15c for LSV scans). (b) IPCE spectra of $Cu_2V_2O_7$ (blue curve) and $Cu_2V_2O_7/CoP_i$ photoanodes (red curve) in 0.3 M K_2SO_4 and 0.2 M phosphate buffer (pH 6.8) at a potential of 1.23 V vs. RHE. All measurements were performed under frontside illumination with Ar bubbling.

Figure S17 shows a Mott–Schottky plot for a 200 nm $Cu_2V_2O_7$ photoanode measured at different frequencies. The positive slope is characteristic of an n-type semiconductor. The flat-band potential (φ_{fb}) is estimated to be 0.61 ± 0.03 V vs. RHE based on the extrapolated x-axis intercepts, which is in excellent agreement with the photocurrent onset potential of the film (~0.65 V vs. RHE). The donor density (N_D) is estimated to be about 6 × 10^{18} cm^{-3} based on the slopes of the Mott–Schottky plots, which is reasonable for an oxide-based semiconductor.[26] The

space charge width (W_{sc}) is estimated to be about 70 nm at 1.23 V vs RHE using equation (7) in the Experimental Section. An open-circuit potential (OCP) measurement under chopped AM1.5 illumination confirms that the films show n-type conductivity, i.e., the OCP shifts to a more negative value upon illumination due to band flattening (see Figure S18).

Chemical composition

In order to determine the chemical and electronic structure of the $Cu_2V_2O_7$ films, XPS and UPS measurements were performed for a 200 nm $Cu_2V_2O_7$ film. No other elements or contaminants (except adventitious carbon) were detected in the survey spectrum (see Figure S2a). Figure 5a shows the Cu $2p_{1/2}$ and Cu $2p_{3/2}$ peaks located at 954.1 and 933.7 eV, respectively, which can be attributed to the Cu^{2+} multiplets, indicating that Cu has a valence state of 2+ in $Cu_2V_2O_7$.[48] The main peak is accompanied by two strong satellites at about 9 eV higher binding energies, which is also consistent with a Cu oxidation state of 2+.[49] The core level spectra of V 2p and O 1s are displayed in Figure 5b. The peaks for V $2p_{3/2}$ (516.7 eV) and V $2p_{1/2}$ (524.3 eV) can be indexed to V^{5+} and the results match well with those reported in the literature.[39, 50] The main O 1s peak occurs at 530.1 eV and is attributed to lattice oxygen. The minor peak at the highest energy of 531.5 eV corresponds to surface adsorbed hydroxyl species, OH.[51]

We also performed XPS on an area of the photocathode that was PEC tested to examine elemental changes during water oxidation. The XPS survey spectrum and the spectra for the Cu 2p, O 1s, V 2p, and C 1s regions are shown in Figure S19. Since there was not a significant difference between the XPS spectra for the pristine and PEC tested samples (other than the higher proportion of the adsorbed hydroxyl species, possibly due to traces of electrolyte), the PEC experiments do not seem to lead to any chemical changes at the surface of the material.

Figure 5c shows the UPS spectrum of a $Cu_2V_2O_7$ film measured with a 2 V bias and a photon energy of 21.21 eV from a He (I) source. The work function, defined as the difference between the vacuum energy level and Fermi level, can be derived from the low kinetic energy cut-off in the secondary emission feature. Given that the Fermi level at the surface of the $Cu_2V_2O_7$ film is considered independently of the spectrometer, the work function is determined to be 21.21 eV – 2 V – 14.1 eV = 5.11 eV. Using 4.5 eV vs. vacuum as the reference value for the electrochemical scale (0.0 V vs. RHE) this places the Fermi level at 0.61 V vs. RHE, which is close to the φ_{fb} value of 0.65 V vs. RHE obtained by the Mott-Schottky analysis. The position of the valence band maximum (VBM) at 1.82 eV below E_F is determined by the linear extrapolation of the UPS spectrum at the low binding energy side to the binding energy axis (see Figure S2c). Our measured band positions are in good agreement with the values reported previously,[17] although we acknowledge that this may be somewhat fortuitous since we cannot rule out that the plasma cleaning treatment (which is needed to reduce the amount of surface-adsorbed carbon species) affects the local surface structure to some extent.

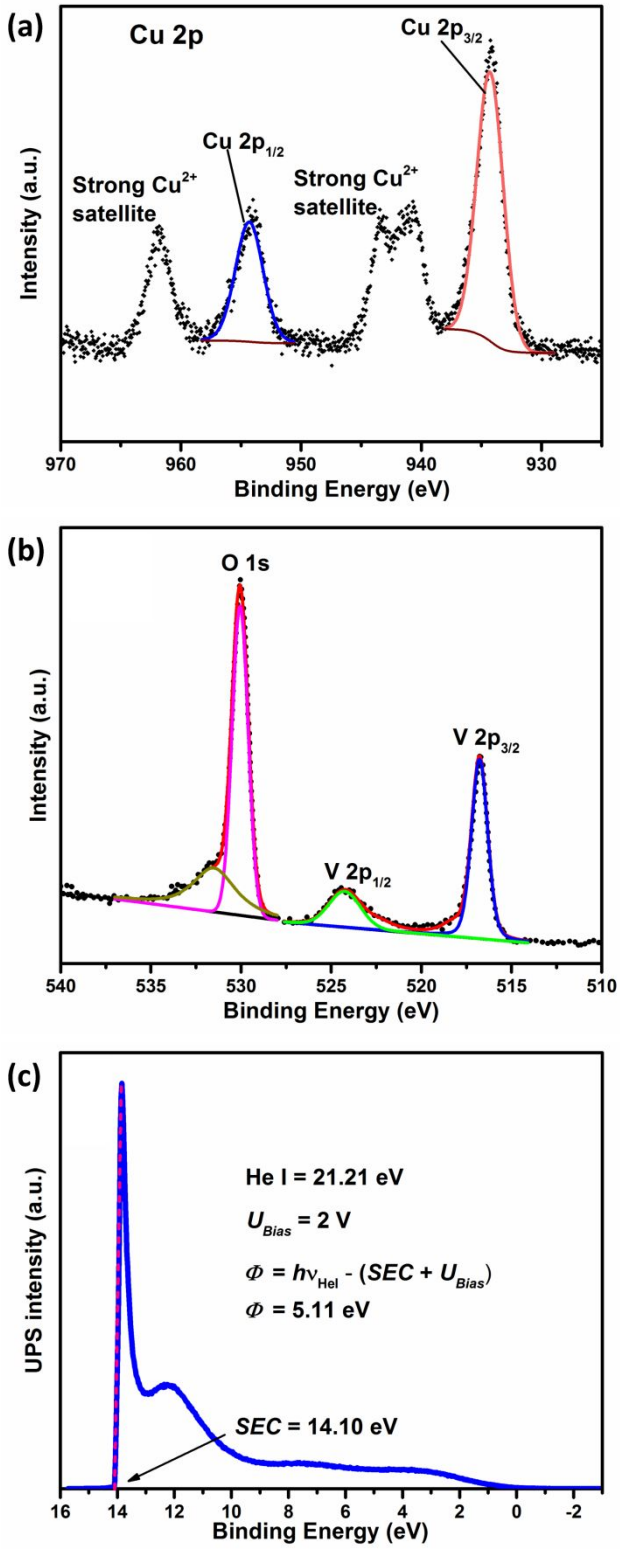

Figure 5. XPS spectra of (a) Cu 2p, (b) V 2p and O 1s for a ~200 nm $Cu_2V_2O_7$ film synthesized by spray-pyrolysis on a FTO substrate and annealed at 500 °C for 2 hours in air. (c)

UPS cutoff spectra of the $Cu_2V_2O_7$ film measured with a 2 V bias.

Based on the UV-vis, Mott-Schottky, and UPS measurements we can now construct a detailed band diagram for β-$Cu_2V_2O_7$. Figure 6 shows the band diagram of our spray deposited $Cu_2V_2O_7$ film with respect to the electrochemical redox potentials for water oxidation (O_2/H_2O) and reduction (H^+/H_2). It shows that the conduction band minimum (CBM) of β-$Cu_2V_2O_7$ is about 500 mV more positive than the H^+/H_2 reduction potential, and the unfavorable conduction band position means that a relatively large external bias voltage is needed to enable hydrogen evolution. The maximum overpotential for the OER, which is given by the position of the valence band edge, is relatively high ($\eta_{OER,max}$ = 1.15 ± 0.1 V). It also shows that the Fermi level of $Cu_2V_2O_7$ is located at -5.1 eV versus the vacuum energy level.

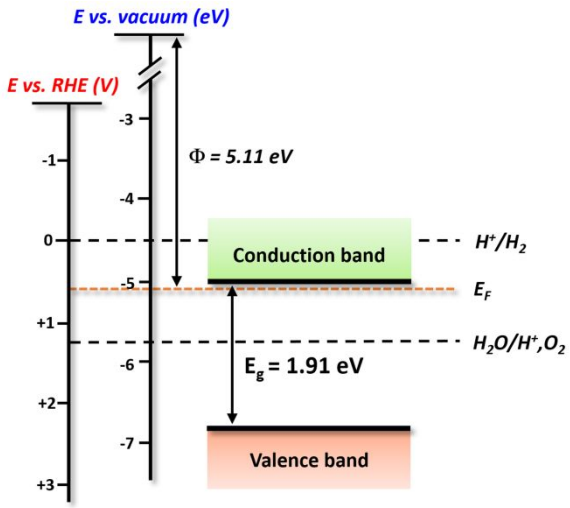

Figure 6. Band diagram for β-$Cu_2V_2O_7$ constructed from UV-vis, Mott–Schottky, and UPS measurements.

Photoelectrochemical Stability and O_2 Production

Stability tests of the $Cu_2V_2O_7/CoP_i$ photoelectrodes have been carried out in an aqueous 0.3 M K_2SO_4 electrolyte with 0.2 M phosphate buffer (pH 6.8) under Ar bubbling. The results are shown in Figure 7a. The photocurrents show an initial fast decay, which can be attributed to either surface recombination or poor catalyst activity. The initial photocurrent may also be due to a surface oxidation process that brings the electrode in equilibrium with the electrolyte under the applied potential. The photocurrent density decreases by 58% within the first 3 min. After this decay, the photocurrent remains stable over the entire 120 min measurement time. For $Cu_2V_2O_7$ photoanodes modified with CoP_i, the photocurrent decreases by only 45% within the first 3 min. We ran LSV scans for $Cu_2V_2O_7$ and $Cu_2V_2O_7/CoP_i$ photoanodes after 120 min PEC stability measurements (see Figure S20), there was no significant drop in photocurrent compared to the data in Figure 4a, indicating that the stability of $Cu_2V_2O_7$ photoanodes was good. After the 120 min photocurrent measurement, the illuminated area of the $Cu_2V_2O_7$ electrode showed no change and was almost indistinguishable from the non-illuminated area (see Figure S21). This means that no significant dissolution occurred. The total photogenerated charge (377 mC/cm^2 for the red curve of Figure 7a) exceeded the corresponding molar amount of $Cu_2V_2O_7$ in the 200 nm thick photoanode by a factor of 1.3. A turn-over number (TON) larger than 1 indicates that at least part of the photocurrent is due to the water oxidation reaction.

During the experiments, gas bubbles were visually observed on the photoanode surface as shown in Figure S22. In order to measure O_2 directly and calculate the faradaic efficiency, electrochemical mass spectrometry (EMS) measurements were performed on the $Cu_2V_2O_7$ photoanode. Figure 7b shows the EMS LSV scans for a 200 nm $Cu_2V_2O_7$ photoanode under illumination. The onset of the current and the O_2 signal from the EMS are 0.2 V mismatched, with the onset in O_2 production occurring around 1.1 V vs RHE. One possible explanation for this is the delayed detection of produced O_2 as it has to travel from the working electrode through a thin electrolyte layer (200 µm) to the membrane-based inlet system of the mass spectrometer. Another possible reason is that there is another oxidation process between 0.9 and 1.1 V_{RHE} on the surface before the OER starts, such as pre-oxidation of the CoP_i catalyst. An EMS LSV control experiment for a 200 nm $Cu_2V_2O_7$ photoanode without illumination is also performed (see Figure S23). In the dark the current and O_2 gas signal are essentially flat. This confirms that the oxygen signal in Figure 7b is entirely due to a photo-electrochemical reaction. To calculate the faradaic efficiency, the sample was kept at a constant potential of 1.5 V vs RHE while recording the current and the O_2 signal of the mass spectrometer. After 5 min, the potential was switched on for 15 min, resulting in a clear increase in photocurrent and O_2 signal (Figure S24). The amount of photogenerated charge was compared to the total molar amount of generated oxygen (using the calibration data in Figure S5), from which a faradaic efficiency ($\eta_{Faradaic}$) of 96% is calculated for the O_2 evolution reaction.

CONCLUSIONS

In this work we have determined several key optoelectronic and photoelectrochemical properties of β-$Cu_2V_2O_7$ photoanodes synthesized by a facile spray pyrolysis method (see Table 1). Previous reports on β-$Cu_2V_2O_7$ photoanodes have shown relatively low photoconversion efficiencies, but the factors that limit the material's performance were not yet fully understood. Our study shows that one of these limitations is the modest optical absorption coefficient of $Cu_2V_2O_7$. Even in the absence of recombination, a 200 nm thick $Cu_2V_2O_7$ film can only generate a photocurrent of 6.5 mA/cm^2; the remaining 57% of the theoretical solar photocurrent of 15 mA/cm^2 for $Cu_2V_2O_7$ will be transmitted without being absorbed. Moreover, the pronounced spectral mismatch between the optical absorption and the quantum efficiency for photocurrent generation suggests a wavelength-dependent photogeneration yield. Specifically, the first

electronic transition is a Cu d→d transition that is unlikely to contribute significantly to the photocurrent. The modest overall absorption cannot be overcome by simply making the films thicker, as is normally done for weakly absorbing semiconductors like silicon. The reason for this is the extensive carrier recombination due to trapping and detrapping, which results in a modest effective carrier diffusion length. These combined effects limit the photocurrent density to about 0.1 mA/cm^2 at 1.23 V vs RHE for our best-performing $Cu_2V_2O_7$ photoanode, even with CoP_i as a catalyst. From an energetic point of view, the main limitation is the relatively positive conduction band minimum. On a more positive note, the main advantage of β-$Cu_2V_2O_7$ is its very good chemical stability, which is unusual for a Cu-containing oxide-based photoelectrode material.

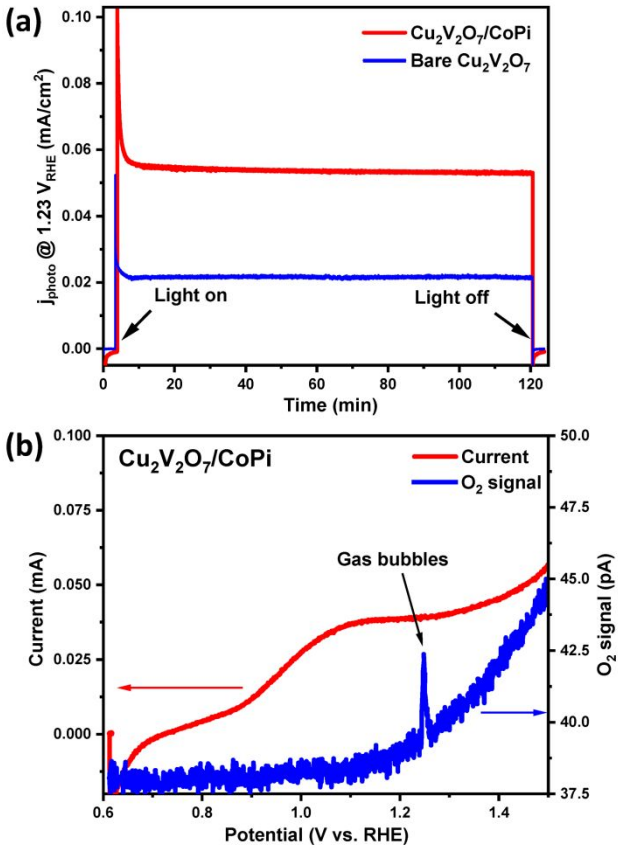

Figure 7. (a) Constant potential measurement at 1.23 V vs RHE for 200 nm $Cu_2V_2O_7$ and $Cu_2V_2O_7/CoP_i$ films in the dark and under (frontside) AM1.5 irradiation. (b) EMS LSV scans (5 mV/s) for a 200 nm $Cu_2V_2O_7$ photoanode under backside illumination, showing the current (red) and the O_2 mass signal (blue). All measurements were done in 0.3 M K_2SO_4 and 0.2 M phosphate buffer (pH 6.8) under Ar bubbling.

To further improve the photoconversion efficiency, several strategies can be pursued. While the CoP_i layer was found to double the photocurrent, other catalyst layers might lead to even larger improvements by either enhancing the charge transfer kinetics or by passivating surface defects.[52]

Although the photocurrent showed excellent stability over a 2-hour period, the faradaic efficiency was slighly less than unity (96%) suggesting that some degradation may occur. To avoid this, suitable protection layers may further improve the stability.[53] Nanostructuring can be used to overcome the mismatch between carrier transport and optical absorption, while doping may enhance the electronic conductivity and charge transport in the films. Similar strategies have been successfully applied to other metal oxide photoelectrode materials, such as $CuBi_2O_4$, Fe_2O_3, $BiVO_4$, and Cu_2O, and are likely to improve the PEC performance of $Cu_2V_2O_7$ as well.[54-58] In view of the very low IPCE values, however, we would encourage the community to spend their efforts on other, more promising candidate materials instead.

Table 1. Summary of Key PEC Parameters of β-$Cu_2V_2O_7$

parameter	value
band gap energy, E_g	1.91 ± 0.05 eV (indirect) 2.05 ± 0.05 eV (direct)
absorption coefficient, α	
at 400 nm:	(4.70 ± 0.36) × 10^4 cm^{-1}
at 450 nm:	(3.35 ± 0.14) × 10^4 cm^{-1}
at 500 nm:	(2.51 ± 0.10) × 10^4 cm^{-1}
at 550 nm:	(1.59 ± 0.09) × 10^4 cm^{-1}
at 600 nm:	(8.19 ± 0.50) × 10^3 cm^{-1}
carrier mobility, μ	3.5 × 10^{-3} cm^2 V^{-1} s^{-1}
Effective carrier lifetime, τ	80 ns
Effective carrier diffusion length, $L_{D,eff}$	28 nm
flat band potential, φ_{fb}	0.61 ± 0.03 V vs. RHE
work function, Φ	5.11 eV vs. Vac
valence band maximum, VBM	2.45 ± 0.03 V vs. RHE
O_2 evolution faradaic efficiency, η_F	96%

ASSOCIATED CONTENT

Supporting Information.
Electrodeposition chronoamperometry curves, continuous and chopped-light LSV scans, XPS spectra, IPCE and APCE measurements, optical power spectrum, electrochemical impedance data, DEMS data, XRD patterns, sample photographs, SEM images, EDX elemental mapping data, AFM images, optical absorption data, time-resolved microwave conductivity data, Mott-Schottky measurements, open circuit potential measurements.

AUTHOR INFORMATION

Corresponding Author

*(R.v.d.K) Email: roel.vandekrol@helmholtz-berlin.de

Author Contributions

The manuscript was written through contributions of all authors. All authors have given approval to the final version of the manuscript.

Funding Sources

China Scholarship Council (File No. 201607040078). Part of this work was funded by the German Bundesministerium für Bildung and Forschung (BMBF), project "MeOx4H2" (03SF0478A).

Notes

The authors declare no competing financial interest.

ACKNOWLEDGMENTS

Angang Song thanks the China Scholarship Council for financial support. We thank Paul Plate for assistance with XPS and UPS measurements and Alexander Esau for the mass spectrometry measurements.

ABBREVIATIONS

PEC, photoelectrochemical; XRD, X-ray diffraction; SEM, scanning electron microscopy; AFM, atomic force microscope; UV-vis, UV-visible light; TRMC, time resolved microwave conductivity; IPCE, incident-photon-to current efficiency; XPS, X-ray photoelectron spectroscopy; UPS, ultraviolet photoelectron spectroscopy; RHE, reversible hydrogen electrode; OER, oxygen evolution reaction; VBM, valence band maximum; Spray pyrolysis deposition; STH, solar-to-hydrogen; LSV, linear sweep voltammograms; OCP, open circuit potential

REFERENCES

(1) Sivula, K.; van de Krol, R., Semiconducting materials for photoelectrochemical energy conversion. *Nat. Rev. Mater.* **2016,** *1*, 15010.

(2) van de Krol, R.; Grätzel, M., *Photoelectrochemical hydrogen production*. Springer: New York, 2012.

(3) Walter, M. G.; Warren, E. L.; McKone, J. R.; Boettcher, S. W.; Mi, Q.; Santori, E. A.; Lewis, N. S., Solar Water Splitting Cells. *Chem. Rev.* **2010,** *110* (11), 6446-6473.

(4) Bak, T.; Nowotny, J.; Rekas, M.; Sorrell, C. C., Photo-electrochemical hydrogen generation from water using solar energy. Materials-related aspects. *Int. J. Hydrogen Energy* **2002,** *27* (10), 991-1022.

(5) Alfaifi, B.; Ullah, H.; Alfaifi, S.; Tahir, A.; Mallick, T., Photoelectrochemical solar water splitting: From basic principles to advanced devices. *Veruscript Funct. Nanomater.* **2018**, 2: #BDJOC3. DOI:10.22261/FNAN.BDJOC3

(6) Hu, S.; Lewis, N. S.; Ager, J. W.; Yang, J.; McKone, J. R.; Strandwitz, N. C., Thin-Film Materials for the Protection of Semiconducting Photoelectrodes in Solar-Fuel Generators. *J. Phys. Chem. C* **2015,** *119* (43), 24201-24228.

(7) Abdi, F. F.; Berglund, S. P., Recent developments in complex metal oxide photoelectrodes. *J. Phys. D: Appl. Phys.* **2017,** *50* (19), 193002.

(8) Kim, T. W.; Choi, K.-S., Nanoporous $BiVO_4$ Photoanodes with Dual-Layer Oxygen Evolution Catalysts for Solar Water Splitting. *Science* **2014,** *343* (6174), 990.

(9) Kim, T. W.; Ping, Y.; Galli, G. A.; Choi, K.-S., Simultaneous enhancements in photon absorption and charge transport of bismuth vanadate photoanodes for solar water splitting. *Nat. Commun.* **2015,** *6*, 8769.

(10) Peter, L. M.; Wijayantha, K. G. U., Photoelectrochemical Water Splitting at Semiconductor Electrodes: Fundamental Problems and New Perspectives. *ChemPhysChem* **2014,** *15* (10), 1983-1995.

(11) Yan, Q.; Yu, J.; Suram, S. K.; Zhou, L.; Shinde, A.; Newhouse, P. F.; Chen, W.; Li, G.; Persson, K. A.; Gregoire, J. M., Solar fuels photoanode materials discovery by integrating high-throughput theory and experiment. *Proc. Natl. Acad. of Sci.* **2017,** *114* (12), 3040-3043.

(12) Jiang, C.-M.; Segev, G.; Hess, L. H.; Liu, G.; Zaborski, G.; Toma, F. M.; Cooper, J. K.; Sharp, I. D., Composition-Dependent Functionality of Copper Vanadate Photoanodes. *ACS Appl. Mater. Interfaces* **2018,** *10* (13), 10627-10633.

(13) Zhou, L.; Yan, Q.; Shinde, A.; Guevarra, D.; Newhouse, P. F.; Becerra-Stasiewicz, N.; Chatman, S. M.; Haber, J. A.; Neaton, J. B.; Gregoire, J. M., High Throughput Discovery of Solar Fuels Photoanodes in the CuO-V_2O_5 System. *Adv. Energy Mater.* **2015,** *5* (22), 1500968.

(14) Hughes, J. M.; Birnie, R. W., Ziesite, β-$Cu_2V_2O_7$, a new copper vanadate and fumarole temperature indicator. *Am. Mineral.* **1980,** *65* (11-12), 1146-1149.

(15) Gadiyar, C.; Strach, M.; Schouwink, P.; Loiudice, A.; Buonsanti, R., Chemical transformations at the nanoscale: nanocrystal-seeded synthesis of β-$Cu_2V_2O_7$ with enhanced photoconversion efficiencies. *Chem. Sci.* **2018,** *9* (25), 5658-5665.

(16) Hassan, A.; Iqbal, T.; Tahir, M. B.; Afsheen, S., A review on copper vanadate-based nanostructures for photocatalysis energy production. *Int. J. Energy Res.* **2018,** *43* (1), 9-28.

(17) Guo, W.; Chemelewski, W. D.; Mabayoje, O.; Xiao, P.; Zhang, Y.; Mullins, C. B., Synthesis and Characterization of CuV_2O_6 and $Cu_2V_2O_7$: Two Photoanode Candidates for Photoelectrochemical Water Oxidation. *J. Phys. Chem. C* **2015,** *119* (49), 27220-27227.

(18) Kim, M.-W.; Joshi, B.; Yoon, H.; Ohm, T. Y.; Kim, K.; Al-Deyab, S. S.; Yoon, S. S., Electrosprayed copper hexaoxodivanadate (CuV_2O_6) and pyrovanadate ($Cu_2V_2O_7$) photoanodes for efficient solar water splitting. *J. Alloys Comp.* **2017,** *708*, 444-450.

(19) Lumley, M. A.; Choi, K.-S., Investigation of Pristine and (Mo, W)-Doped $Cu_{11}V_6O_{26}$ for Use as Photoanodes for Solar Water Splitting. *Chem. Mater.* **2017,** *29* (21), 9472-9479.

(20) Hossain, M. K.; Sotelo, P.; Sarker, H. P.; Galante, M. T.; Kormányos, A.; Longo, C.; Macaluso, R. T.; Huda, M. N.; Janáky, C.; Rajeshwar, K., Rapid One-Pot Synthesis and Photoelectrochemical Properties of Copper Vanadates. *ACS Appl. Energy Mater.* **2019,** *2* (4), 2837-2847.

(21) Benko, F. A.; Koffyberg, F. P., Semiconductivity and optical interband transitions of CuV_2O_6 and $Cu_2V_2O_7$. *Can. J. Phys.* **1992,** *70* (2-3), 99-103.

(22) Seabold, J. A.; Neale, N. R., All First Row Transition Metal Oxide Photoanode for Water Splitting Based on $Cu_3V_2O_8$. *Chem. Mater.* **2015,** *27* (3), 1005-1013.

(23) Jiang, C.-M.; Farmand, M.; Wu, C. H.; Liu, Y.-S.; Guo, J.; Drisdell, W. S.; Cooper, J. K.; Sharp, I. D., Electronic Structure, Optoelectronic Properties, and Photoelectrochemical Characteristics of γ-$Cu_3V_2O_8$ Thin Films. *Chem. Mater.* **2017,** *29* (7), 3334-3345.

(24) Abdi, F. F.; van de Krol, R., Nature and Light Dependence of Bulk Recombination in Co-Pi-Catalyzed $BiVO_4$ Photoanodes. *J. Phys. Chem. C* **2012,** *116* (17), 9398-9404.

(25) Zhong, D. K.; Choi, S.; Gamelin, D. R., Near-Complete Suppression of Surface Recombination in Solar Photoelectrolysis by "Co-Pi" Catalyst-Modified W:$BiVO_4$. *J. Am. Chem. Soc.* **2011,** *133* (45), 18370-18377.

(26) Song, A.; Plate, P.; Chemseddine, A.; Wang, F.; Abdi, F. F.; Wollgarten, M.; van de Krol, R.; Berglund, S. P., Cu:NiO as a hole-selective back contact to improve the photoelectrochemical performance of $CuBi_2O_4$ thin film photocathodes. *J. Mater. Chem. A* **2019,** *7* (15), 9183-9194.

(27) Sannigrahi, J.; Bhowal, S.; Giri, S.; Majumdar, S.; Dasgupta, I., Exchange-striction induced giant ferroelectric polarization in copper-based multiferroic material. *Phys. Rev. B* **2015,** *91* (22), 220407.

(28) Slobodin, B. V.; Samigullina, R. F., Thermoanalytical study of the polymorphism and melting behavior of $Cu_2V_2O_7$. *Inorg. Mater.* **2010,** *46* (2), 196-200.

(29) Schindler, M.; Hawthorne, F. C., Structural Characterization of the β-$Cu_2V_2O_7$–α-$Zn_2V_2O_7$ Solid Solution. *J. Solid State Chem.* **1999,** *146* (1), 271-276.
(30) Cherepansky, P. N.; Krivovichev, S. V.; Filatov, S. K.; Armbruster, T.; Pankratova, O. Y., Crystal Structure of γ-$Cu_2V_2O_7$ and its comparison to blossite (α-$Cu_2V_2O_7$) and ziesite (β-$Cu_2V_2O_7$). *Can. Mineral.* **2005,** *43* (2), 671-677.
(31) Yashima, M.; Suzuki, R. O., Electronic structure and magnetic properties of monoclinic β-$Cu_2V_2O_7$: a GGA+U study. *Phys. Rev. B* **2009,** *79* (12).
(32) Newhouse, P.; Boyd, D.; Shinde, A.; Guevarra, D.; Zhou, L.; Soedarmadji, E.; Li, G.; Neaton, J. B.; Gregoire, J. M., Solar fuel photoanodes prepared by inkjet printing of copper vanadates. *J. Mater. Chem. A* **2016,** *4* (19), 7483-7494.
(33) Shuang, S.; Girardi, L.; Rizzi, G. A.; Sartorel, A.; Marega, C.; Zhang, Z.; Granozzi, G., Visible Light Driven Photoanodes for Water Oxidation Based on Novel r-GO/β-$Cu_2V_2O_7$/TiO_2 Nanorods Composites. *Nanomaterials* **2018,** *8* (7), 544.
(34) de Waal, D.; Hutter, C., Vibrational spectra of two phases of copper pyrovanadate and some solid solutions of copper and magnesium pyrovanadate. *Mater. Res. Bull.* **1994,** *29* (8), 843-849.
(35) Wiktor, J.; Reshetnyak, I.; Strach, M.; Scarongella, M.; Buonsanti, R.; Pasquarello, A., Sizable Excitonic Effects Undermining the Photocatalytic Efficiency of beta-$Cu_2V_2O_7$. *J. Phys. Chem. Lett.* **2018,** *9* (19), 5698-5703.
(36) Berglund, S. P.; Abdi, F. F.; Bogdanoff, P.; Chemseddine, A.; Friedrich, D.; van de Krol, R., Comprehensive Evaluation of $CuBi_2O_4$ as a Photocathode Material for Photoelectrochemical Water Splitting. *Chem. Mater.* **2016,** *28* (12), 4231-4242.
(37) Abdi, F. F.; Chemseddine, A.; Berglund, S. P.; van de Krol, R., Assessing the Suitability of Iron Tungstate (Fe_2WO_6) as a Photoelectrode Material for Water Oxidation. *J. Phys.Chem. C* **2017,** *121* (1), 153-160.
(38) Kölbach, M.; Pereira, I. J.; Harbauer, K.; Plate, P.; Höflich, K.; Berglund, S. P.; Friedrich, D.; van de Krol, R.; Abdi, F. F., Revealing the Performance-Limiting Factors in α-$SnWO_4$ Photoanodes for Solar Water Splitting. *Chem. Mater.* **2018,** *30* (22), 8322-8331.
(39) Zhang, M.; Ma, Y.; Friedrich, D.; van de Krol, R.; Wong, L. H.; Abdi, F. F., Elucidation of the opto-electronic and photoelectrochemical properties of $FeVO_4$ photoanodes for solar water oxidation. *J. Mater. Chem. A* **2018,** *6* (2), 548-555.
(40) Ravensbergen, J.; Abdi, F. F.; van Santen, J. H.; Frese, R. N.; Dam, B.; van de Krol, R.; Kennis, J. T. M., Unraveling the Carrier Dynamics of $BiVO_4$: A Femtosecond to Microsecond Transient Absorption Study. *J. Phys. Chem. C* **2014,** *118* (48), 27793-27800.
(41) Sher, P. H.; Smith, J. M.; Dalgarno, P. A.; Warburton, R. J.; Chen, X.; Dobson, P. J.; Daniels, S. M.; Pickett, N. L.; O'Brien, P., Power law carrier dynamics in semiconductor nanocrystals at nanosecond timescales. *Appl. Phys. Lett.* **2008,** *92* (10), 101111
(42) Kroeze, J. E.; Savenije, T. J.; Warman, J. M., Electrodeless Determination of the Trap Density, Decay Kinetics, and Charge Separation Efficiency of Dye-Sensitized Nanocrystalline TiO_2. *J. Am. Chem. Soc.* **2004,** *126* (24), 7608-7618.
(43) Kuno, M.; Fromm, D. P.; Hamann, H. F.; Gallagher, A.; Nesbitt, D. J., Nonexponential "blinking" kinetics of single CdSe quantum dots: A universal power law behavior. *J. Phys.Chem. C* **2000,** *112* (7), 3117-3120.
(44) Barzykin, A.; Tachiya, M., Mechanism of charge recombination in dye-sensitized nanocrystalline semiconductors: random flight model. *J. Phys.Chem. B* **2002,** *106* (17), 4356-4363.
(45) Kay, A.; Fiegenbaum-Raz, M.; Müller, S.; Eichberger, R.; Dotan, H.; van de Krol, R.; Abdi, F. F.; Rothschild, A.; Friedrich, D.; Grave, D. A., Effect of Doping and Excitation Wavelength on Charge Carrier Dynamics in Hematite by Time-Resolved Microwave and Terahertz Photoconductivity. *Adv. Funct. Mater.* **2019**, 1901590.
(46) Carneiro, L. M.; Cushing, S. K.; Liu, C.; Su, Y.; Yang, P.; Alivisatos, A. P.; Leone, S. R., Excitation-wavelength-dependent small polaron trapping of photoexcited carriers in α-Fe_2O_3. *Nat. Mater.* **2017,** *16*, 819.
(47) Hayes, D.; Hadt, R. G.; Emery, J. D.; Cordones, A. A.; Martinson, A. B. F.; Shelby, M. L.; Fransted, K. A.; Dahlberg, P. D.; Hong, J.; Zhang, X.; Kong, Q.; Schoenlein, R. W.; Chen, L. X., Electronic and nuclear contributions to time-resolved optical and X-ray absorption spectra of hematite and insights into photoelectrochemical performance. *Energy Environ. Sci.* **2016,** *9* (12), 3754-3769.
(48) Gan, Z. H.; Yu, G. Q.; Tay, B. K.; Tan, C. M.; Zhao, Z. W.; Fu, Y. Q., Preparation and characterization of copper oxide thin films deposited by filtered cathodic vacuum arc. *J. Phys. D: Appl. Phys.* **2003,** *37* (1), 81-85.
(49) Ghijsen, J.; Tjeng, L. H.; van Elp, J.; Eskes, H.; Westerink, J.; Sawatzky, G. A.; Czyzyk, M. T., Electronic structure of Cu_2O and CuO. *Phys. Rev. B* **1988,** *38* (16), 11322-11330.
(50) Liu, Y.; Guo, Y.; Schelhas, L. T.; Li, M.; Ager, J. W., Undoped and Ni-Doped CoO_x Surface Modification of Porous $BiVO_4$ Photoelectrodes for Water Oxidation. *J. Phys. Chem. C* **2016,** *120* (41), 23449-23457.
(51) Szuber, J.; Czempik, G.; Larciprete, R.; Koziej, D.; Adamowicz, B., XPS study of the L-CVD deposited SnO_2 thin films exposed to oxygen and hydrogen. *Thin Solid Films* **2001,** *391* (2), 198-203.
(52) Zachäus, C.; Abdi, F. F.; Peter, L. M.; van de Krol, R., Photocurrent of $BiVO_4$ is limited by surface recombination, not surface catalysis. *Chem. Sci.* **2017,** *8* (5), 3712-3719.
(53) Lee, D. K.; Lee, D.; Lumley, M. A.; Choi, K.-S., Progress on ternary oxide-based photoanodes for use in photoelectrochemical cells for solar water splitting. *Chem. Soc. Rev.* **2019,** *48* (7), 2126-2157.
(54) Wang, F.; Septina, W.; Chemseddine, A.; Abdi, F. F.; Friedrich, D.; Bogdanoff, P.; van de Krol, R.; Tilley, S. D.; Berglund, S. P., Gradient Self-Doped $CuBi_2O_4$ with Highly Improved Charge Separation Efficiency. *J. Am. Chem. Soc.* **2017,** *139* (42), 15094-15103.
(55) Li, C.; Hisatomi, T.; Watanabe, O.; Nakabayashi, M.; Shibata, N.; Domen, K.; Delaunay, J.-J., Positive onset potential and stability of Cu_2O-based photocathodes in water splitting by atomic layer deposition of a Ga_2O_3 buffer layer. *Energy Environ. Sci.* **2015,** *8* (5), 1493-1500.
(56) Lee, D. K.; Choi, K.-S., Enhancing long-term photostability of $BiVO_4$ photoanodes for solar water splitting by tuning electrolyte composition. *Nat. Energy* **2018,** *3* (1), 53.
(57) Kang, D.; Hill, J. C.; Park, Y.; Choi, K.-S., Photoelectrochemical Properties and Photostabilities of High Surface Area $CuBi_2O_4$ and Ag-Doped $CuBi_2O_4$ Photocathodes. *Chem. Mater.* **2016,** *28* (12), 4331-4340.
(58) Jian, J.; Jiang, G.; van de Krol, R.; Wei, B.; Wang, H. Recent Advances in Rational Engineering of Multinary Semiconductors for Photoelectrochemical Hydrogen Generation. *Nano Energy* **2018**, 51, 457–480.

For Table of Contents Only